INO80 regulates chromatin accessibility to facilitate meiotic sex chromosome inactivation

Prabuddha Chakraborty[1], Terry Magnuson[1,2]

[1]Department of Genetics, [2]Lineberger Comprehensive Cancer Center, University of North Carolina at Chapel Hill, Chapel Hill, NC 27599-7264, USA

Corresponding author:

Terry Magnuson
5022, Genetic Medicine Building
120 Mason Farm Road
Chapel Hill, NC 27599-7264
Telephone: 919-843-4678, Fax: 919-843-4682
Email: tmagnuson@unc.edu

Running title: INO80 regulates meiotic sex chromosome inactivation in spermatocytes

Keywords: Spermatogenesis, Chromatin remodeler, INO80, MDC1, Chromatin accessibility, Meiotic sex chromosome inactivation (MSCI).

Abstract

The INO80 protein is the main catalytic subunit of the INO80-chromatin remodeling complex, which is critical for DNA repair and transcription regulation in murine spermatocytes. In this study, we explored the role of INO80 in silencing genes on meiotic sex chromosomes. Robust INO80 immunolocalization at the XY body in pachytene spermatocytes suggested a role for INO80 in the meiotic sex body. Subsequent deletion of *Ino80* resulted in high expression of sex-linked genes. Furthermore, the active form of RNA polymerase II at the sex body of *Ino80*-null pachytene spermatocytes indicates incomplete meiotic sex chromosome inactivation (MSCI). A reduction in the recruitment of MSCI initiators argues for INO80-facilitated recruitment of DNA repair factors required for MSCI initiation. This role of INO80 is independent of a common INO80 target H2A.Z. Instead, in the absence of INO80, a reduction in chromatin accessibility at DNA repair sites occurs on the sex chromosomes. These data suggest a unique role for INO80 in DNA repair factor localization, thereby facilitating the silencing of sex-linked genes during the onset of pachynema.

Introduction

Mammalian gametogenesis involves the meiotic division of diploid germ cells that undergo homologous chromosome synapsis and recombination to generate haploid gametes. Extended prophase I during meiosis ensures the faithful execution of recombination to shuffle genetic material between homologous chromosomes by controlled introduction of DNA double-strand breaks (DDSB) followed by their repair (Handel and Schimenti, 2010). Synapsis between homologous autosomes occurs

during the zygotene stage of meiotic prophase I. In contrast, non-homologous regions of the X and Y sex chromosomes in male germ cells do not synapse with each other (Burgoyne and Baker, 1985).

During pachynema, DNA double-strand break repair (DSBR) factors no longer localize to autosomes indicating completion of DSBR. For the sex chromosomes, the DSBR factors sequester at unpaired regions, forming a unique chromatin domain called the sex body (Solari, 1964; Yan and McCarrey, 2009). The sex chromosomes undergo an extensive chromatin remodeling process to induce epigenetic silencing of sex-linked genes. This process is known as meiotic sex chromosome inactivation (MSCI) (Turner, 2015). Incomplete MSCI leads to germ cell death during pachynema causing male infertility (Turner, 2015).

The sex chromosomes in spermatocytes undergo modifications by several DNA damage repair (DDR) factors such as BRCA1, ATR, and its activator TOPBP1 at the unpaired (asynapsed) chromosome axes (Turner et al., 2004). MSCI initiates by DNA double-strand breaks (DSB) at the asynapsed axes and the incorporation of DSBR proteins at these DSB sites (Carofiglio et al., 2013; Schoenmakers et al., 2008). ATR localizes to the DSBs along the chromosome axes (Royo et al., 2013). Serine-139 phosphorylation of H2A.X (γH2A.X) at the DSBs by ATR leads to the recruitment of another DSB factor, MDC1 (Ichijima et al., 2011a; Royo et al., 2013; Stewart et al., 2003; Stucki et al., 2005). MDC1 localization amplifies γH2A.X in the protruding chromatin loops along the axes, resulting in the establishment of the characteristic sex-body and MSCI (Ichijima et al., 2011a; Ichijima et al., 2012).

73 Chromatin remodelers are critical regulators of chromatin accessibility. They play vital
74 roles in several cellular processes, including DNA repair and transcription regulation.
75 Chromatin remodeling enzymes can hydrolyze ATP to change chromatin conformation
76 by moving, evicting, or incorporating nucleosomes. They can also facilitate specific
77 histone variant exchange to change local chromatin accessibility. There are four major
78 families of chromatin remodeling complexes, all of which play critical functions in murine
79 spermatogenesis (Dowdle et al., 2013; Imai et al., 2020; Kim et al., 2012; Li et al., 2014;
80 Serber et al., 2016; Spruce et al., 2020; Wang et al., 2012). However, it is unclear
81 whether chromatin remodelers play any role in the meiotic silencing of the sex
82 chromosomes.

83 Here, we explore the role of INO80 in silencing meiotic sex chromosomes. We show
84 that INO80 interacts with and regulates sex-linked gene silencing in pachytene
85 spermatocytes. Further, INO80 promotes the opening of the sex chromatin during the
86 zygonema-to-pachynema transition. INO80 also facilitates the interaction of DNA repair
87 factors at the DSB sites and interacts with DSBR factors to facilitate the silencing of sex
88 chromosomes.

89 Results

90 INO80 localizes to the sex chromosomes in meiotic germ cells

91 Immunofluorescence localization of INO80 in pachytene spermatocytes revealed robust
92 staining on the sex chromosomes (Fig. 1A, B). Chromatin immunoprecipitation followed
93 by high throughput sequencing (ChIP-seq) for INO80 (GEO Dataset GSE179584)
94 (Chakraborty and Magnuson, 2022) also showed binding on the sex chromosomes (Fig.

95 1C). INO80 binding occurred at the zygotene and pachytene stages (GEO Dataset
96 GSE190590) (Carbajal et al., 2022). However, localization is more enriched at the
97 postnatal day 18 (P18) pachytene stage (Fig. 1C). Additionally, INO80 binding sites on
98 sex chromosomes are present at the DSB sites identified by the meiotic DSB marker
99 γH2A.X. These binding sites include promoter and intergenic regions and gene bodies
100 (Fig. S1). These data suggested a possible role of INO80 in silencing the expression of
101 genes on the sex chromosomes.

102 **INO80 regulates sex chromosome silencing in pachytene spermatocytes**

103 RNAseq analysis of changes in P18 transcription from autosomes in wild type
104 (*Ino80*WT) and germ cell-specific *Ino80*-null (*Ino80*cKO) spermatocytes (GEO Dataset
105 GSE179584) revealed up-and down-regulated genes (padj< 0.05). However, the mean
106 changes in expression remained close to zero (Fig. 2A). In contrast, the differentially
107 expressed genes (DEGs) (padj< 0.05) from the X- and Y- chromosomes remained
108 upregulated in *Ino80*cKO cells (Fig. 2A). When plotted along the length of three
109 representative autosomes and the sex chromosomes, like autosomal genes, DEGs from
110 sex chromosomes occur along the length of the chromosomes (Fig. 2C). We further
111 validated the upregulation of five representative sex-linked genes (*Ccnb3, Nxt2, Eda2r,*
112 *Abcd1, Usp11*) in *Ino80*cKO spermatocytes by qRT-PCR analysis (Fig. 2B). These data
113 corroborated our RNAseq data.

114 Consistent with transcriptional silencing, immunofluorescence analysis of the active
115 form of RNA polymerase II (pSer2) revealed its absence at the sex chromosomes in
116 *Ino80*WT pachytene spermatocytes (Fig. 2D). These data correlate with normal
117 transcriptional silencing. In contrast, continued RNA polymerase II (pSer2)

118 immunofluorescence in *Ino80*cKO pachytene spermatocytes indicates incomplete
119 silencing of the sex-linked genes (Fig. 2D).

120 **INO80 is necessary for the localization of DSBR factors to sex chromosomes**

121 DSBR factors such as ATR, γH2A.X, and MDC1 are required to initiate meiotic sex
122 chromosome inactivation in pachytene spermatocytes (Fernandez-Capetillo et al., 2003;
123 Ichijima et al., 2011a; Royo et al., 2013). We explored the localization of these DSBR
124 proteins in P21 wild-type and mutant pachytene spermatocytes. Complete sequestration
125 of ATR occurred on early *Ino80*WT pachytene sex chromosomes (Fig. 3A). In contrast,
126 ATR lacked localization on the sex chromosomes of early to mid-pachytene *Ino80*cKO
127 spermatocytes. We tested the activity of ATR by immunostaining for the ATR substrate
128 phospho-CHK1 (S345) (Fedoriw et al., 2015). Although the localization of pCHK1
129 (S345) was limited to the sex chromosomes in *Ino80*WT pachytene spermatocytes,
130 aberrant localization occurred in *Ino80*cKO autosomes (Fig. 3B). These data indicate
131 active DNA binding and kinase activity of ATR in the *Ino80*cKO spermatocytes.

132 During pachynema progression, the amplification of ATR-mediated phosphorylation of
133 H2A.X depends on MDC1 recruitment (Ichijima et al., 2011a). We next determined
134 MDC1 localization in *Ino80*cKO pachytene spermatocytes. Robust MDC1
135 immunofluorescence was visible on early- to mid-pachynema *Ino80*WT sex
136 chromosomes (Fig. 3C,D). Conversely, reduced staining occurred at the same stages in
137 *Ino80*cKO spermatocytes (Fig. 3C,D). These results indicate that INO80 facilitates the
138 localization of MDC1 at sex chromosome DSBs during pachynema. Further, to
139 determine MDC1 recruitment, we performed cleavage under targets and release using
140 nuclease (CUT&RUN) in *Ino80*WT and *Ino80*cKO spermatocytes. Quantitative PCR

141 analysis revealed a distinct reduction in MDC1 enrichment at several DSB regions
142 marked by γH2A.X binding (obtained from the publicly available dataset GSE75221)
143 (Fayer et al., 2016) (Fig. S2A). These data corroborate our previous observations.
144 Further, we also observed downregulation of MDC1 mRNA and protein in the *Ino80*cKO
145 spermatocytes (Fig. S2B,C). In addition, the enrichment of INO80 at the promoter of
146 *Mdc1* suggests a requirement for INO80 regulation of MDC1 expression (Fig. S2D).

147 To determine whether INO80 physically recruits DSB repair factors, we performed co-
148 immunoprecipitation for INO80 from P21 spermatocytes. The presence of ATR and
149 MDC1 with the INO80-immunoprecipitated samples (Fig. 3E) and the detection of
150 INO80 in MDC1- and ATR-immunoprecipitated samples (Fig. S2E) supports the
151 physical interaction between INO80 and DSBR factors ATR and MDC1. The addition of
152 ethidium bromide to the spermatocyte lysate did not alter either MDC1 or ATR detection
153 in the immunoblot (Fig. 3E). This result indicates the interaction between MDC1 and
154 INO80 is chromatin independent.

155 Because MDC1 is essential for amplifying γH2A.X, we determined whether perturbation
156 of γH2A.X distribution occurred in the *Ino80*cKO spermatocytes. Robust γH2A.X
157 staining was observed spanning the entire sex body in the *Ino80*WT but not the
158 *Ino80*cKO spermatocytes. Instead, a reduction in the γH2A.X signal occurred on the
159 axes of the sex chromosomes (Fig. 4).

160 **INO80 regulates chromatin accessibility at the sex chromosomes**

161 INO80 is capable of histone exchange, most notably removing H2A.Z from chromatin
162 (Brahma et al., 2017; Papamichos-Chronakis et al., 2011). To determine how INO80

163 changes chromatin dynamics on the sex chromosomes, we compared H2A.Z
164 occupancy at sex-linked gene promoters in P18 *Ino80*cKO and *Ino80*WT
165 spermatocytes. Little change in H2A.Z levels occurred at the promoter and
166 transcriptional start sites (TSS) and INO80 binding sites on the sex chromosomes (Fig.
167 S3A-B). These results suggest that H2A.Z is not mediating the effect of INO80 in the
168 sex body. We also examined the occupancy of activating histone modification H3K4me3
169 and suppressive histone modification H3K27me3. Neither of these showed any change
170 (Fig. S3C,D).

171 Chromatin accessibility can be another regulator of DNA-interacting protein binding at
172 the chromatin. A global change in chromatin accessibility occurs in developing
173 spermatocytes during the mitosis-to-meiosis transition and subsequent progression
174 through meiosis (Maezawa et al., 2018). We performed Assay for Transposase-
175 Accessible Chromatin with high-throughput sequencing (ATAC-seq) to determine
176 accessible chromatin distribution in the developing *Ino80*WT spermatocytes at P12
177 (enriched at zygonema) and compared it with ATAC-seq data from P18 *Ino80*WT
178 spermatocytes (enriched at pachynema) (GEO Dataset GSE179584) (Chakraborty and
179 Magnuson, 2022). Chromatin accessibility at promoter/TSS regions in autosomes at
180 both P12 and P18 was higher than that observed for the sex chromosomes (Fig. S4A).
181 Further, a substantial increase in chromatin accessibility occurred at these regions in
182 both autosomes and sex chromosomes from P12 to P18 (Fig. S4A). This increase did
183 not reverse in *Ino80*cKO spermatocytes at P18 (Fig. S4A). These data indicate a lack of
184 requirement for INO80 in generating accessible chromatin at promoter/TSS during this
185 transition. Next, we determined how the distribution of chromatin accessibility changed

186 during the zygonema to pachynema transition. Comparison of sex chromosome-specific
187 ATAC-peaks revealed a small portion of unique sites (1.34%) on P12 spermatocytes.
188 Most P12 peaks remained at P18. The common peaks account for 20% of the P18
189 ATAC peaks from sex chromosomes, while 80% of ATAC peaks at P18 were *de novo* in
190 nature (Fig. S4B). Comparison of ATAC-peaks on sex chromosomes from *Ino80*cKO
191 spermatocytes (GEO Dataset GSE179584) (Chakraborty and Magnuson, 2022)
192 showed only 17% of these *de novo* peaks remain in *Ino80*cKO, and 83% of de novo
193 peaks are lost (Fig. S4B). Further, genomic annotation analysis of these ATAC-peaks
194 from sex chromosomes suggested a significant increase in intronic (9% to 19%) and
195 distal intergenic (24% to 51%) accessible regions during the transition from P12 to P18
196 (Fig. S4C). This result is because 81% of the *de novo* gained peaks occurred in intronic
197 and distal intergenic regions, and only 7% were at promoter/TSS sites (Fig. S4C). In
198 *Ino80*cKO spermatocytes, we observed a loss of a similar distribution of peaks. Most of
199 the binding occurred in intronic and intergenic regions, suggesting that INO80 regulates
200 the generation of these peaks (Fig. S4C).

201 We next performed a chromosome-specific comparison of accessible regions at each
202 peak between P12 and P18 spermatocytes from *Ino80*WT testes. These experiments
203 revealed a significant increase in chromatin accessibility at various locations across
204 autosomes and sex chromosomes (Fig. 5A). All autosomes showed an increase in
205 chromatin accessibility at most of the differentially accessible regions (FDR <0.05) (Fig.
206 5A). However, sex chromosomes, especially the X-chromosome, exhibited a greater
207 degree of increase at all the differentially accessible regions (FDR < 0.05) (Fig. 5A). The
208 genomic location of the differentially accessible sites mainly occurs at the intronic and

209 intergenic areas. At the same time, a minor portion of them occur at promoter-proximal
210 regions (Fig. 5B). The distribution of increased and decreased accessible areas (FDR <
211 0.05) was primarily similar. In contrast, the number of regions with reduced accessibility
212 was minimal. These data indicate that a genome-wide increase in chromatin
213 accessibility occurs during the zygonema to pachynema transition. The increase is more
214 prevalent on the sex chromosomes (Fig. 5A).

215 To determine the role of INO80 in regulating the transition in chromatin accessibility
216 during meiotic progression, we compared the accessible sites in P18 spermatocytes
217 from either *Ino80*WT or *Ino80*cKO spermatocytes (GEO Dataset GSE179584)
218 (Chakraborty and Magnuson, 2022). We observed a minimal change in accessible
219 chromatin at the autosomes. In contrast, most of the differentially accessible regions
220 were located at the sex chromosomes, demonstrating a much larger and significant
221 change in accessibility (Fig. 5C). Genomic annotation analyses suggested that these
222 differentially accessible chromatin regions mainly belong to intronic and intergenic
223 regions (Fig. 5D). This data indicate that INO80 plays a vital role in regulating the
224 increased chromatin accessibility on the sex chromosome during meiotic progression.
225 We next compared ATAC-signal from *Ino80*WT and *Ino80*cKO spermatocytes at the
226 DSB regions marked by γH2A.X binding (obtained from publicly available dataset
227 GSE75221) (Fayer et al., 2016). A significant decrease in chromatin accessibility in
228 *Ino80cKO* suggests a less permissive environment for DSBR factor recruitment at the
229 DSB sites (Fig. 5E). These data indicate an essential role for INO80 in recruiting DNA
230 damage repair factors to sex chromosome DSBs by regulating chromatin accessibility.

231 **Discussion**

232 In this study, we demonstrated a unique role for INO80 in silencing sex-linked genes
233 during pachynema in spermatocytes. INO80 regulates chromatin accessibility at DSB
234 regions of the sex chromosomes. This regulation is independent of the histone variant
235 H2A.Z, a major INO80 effector. We also demonstrated that INO80 interacts with DSBR
236 factors ATR and MDC1, facilitating MDC1 recruitment at the sex chromosomes during
237 pachynema.

238 An earlier report showed that male germ cell-specific deletion of *Ino80* results in a
239 meiotic arrest phenotype in 8-week-old murine testes (Serber et al., 2016). A significant
240 population of spermatocytes displays defects in synapsis. However, at ~3 weeks post-
241 partum, the zygotene and pachytene spermatocyte populations remain similar between
242 *Ino80*WT and *Ino80*cKO testes. In contrast, the absence of INO80 perturbs the
243 transition from pachynema to diplonema (Chakraborty and Magnuson, 2022). We
244 observed a lack of downregulation of sex-linked differentially expressed genes in
245 *Ino80*cKO spermatocytes. Furthermore, active RNA polymerase II at the sex
246 chromosomes corroborates the observation of an incomplete MSCI. Several other
247 studies that describe roles for MSCI-regulating factors also reported similar
248 characteristics (Becherel et al., 2013; Hirota et al., 2018; Ichijima et al., 2011b; Yeo et
249 al., 2015).

250 Several studies have described a regulatory role for INO80 in DNA damage response in
251 somatic cells and meiosis (Morrison, 2017; Poli et al., 2017; Serber et al., 2016). The
252 INO80 chromatin remodeling complex interacts with DNA damage factors such as
253 γH2A.X and MEC1 (ATR) at DSB repair sites in yeast (Morrison et al., 2004; Poli et al.,
254 2016). We also found that INO80 interacts with DNA repair factors ATR and MDC1 in

255 meiotic spermatocytes. γH2A.X recruitment at DSB sites during zygonema remained
256 intact in *Ino80*cKO spermatocytes. We propose that the initial deposition of γH2A.X at
257 the synapse axis of sex chromosomes initiates INO80-facilitated recruitment of MDC1.
258 This recruitment amplifies γH2A.X in chromatin loops in an INO80-facilitated ATR-
259 dependent fashion.

260 INO80 is known to regulate transcription in several cell types. It facilitates the
261 recruitment of RNA polymerase II (RNAPII) and its cofactors to the promoters of
262 pluripotency network genes. This recruitment regulates embryonic stem cell
263 pluripotency and reprogramming (Wang et al., 2014; Zhou et al., 2016). It can also
264 regulate gene expression by facilitating histone modifications and the exchange of
265 histone variants such as H2A.Z in different cell types (Alatwi and Downs, 2015; Brahma
266 et al., 2017; Chakraborty and Magnuson, 2022; Yu et al., 2021). However, INO80-
267 dependent silencing of sex-linked genes in meiotic spermatocytes seems to be
268 independent of INO80-mediated direct transcriptional regulation by enabling DNA
269 binding factor recruitment at the promoter-proximal areas.

270 We showed that INO80 regulates sex chromosome accessibility during meiotic
271 progression. Chromatin accessibility is a central regulator of DNA damage repair
272 response. Less accessible DNA hinders successful and efficient DNA repair
273 (Luijsterburg and Van Attikum, 2011; Price et al., 2013). Chromatin accessibility is also
274 essential in transcription factor recruitment and efficient transcription regulation at the
275 promoter-proximal areas (Allis and Jenuwein, 2016). We observed an increase in
276 overall chromatin accessibility at promoter regions of autosomes and sex
277 chromosomes.

278 In contrast, a similar level of accessibility remains at the promoter-proximal areas of sex
279 chromosomes due to *Ino80 deletion*. Maezawa *et al.* previously reported that the
280 accessibility at the promoter/TSS during the pachynema transition remains relatively
281 unchanged. At the same time, substantial changes in gene expression occur at this time
282 (Maezawa et al., 2018). It is possible that chromatin accessibility is dynamically
283 controlled and changes substantially between stages during spermatogenesis.
284 Additionally, the *de novo* generation of ATAC-seq peaks may explain gene silencing
285 during MSCI. Further, INO80 appears to be a central regulator of this process by
286 regulating this *de novo* accessibility generation, as most of these peaks are lost in
287 *Ino80*cKO spermatocytes. The loss of accessibility at the γH2A.X-binding DSB regions
288 due to *Ino80* deletion also indicates a possible INO80-dependent recruiting mechanism
289 for DSBR factors such as MDC1.

290 Here we propose that INO80 mediates the *de novo* opening of chromatin around the
291 DSB regions and facilitates recruitment of MDC1, whereby MDC1 initiates γH2A.X
292 amplification by enabling ATR recruitment (Fig. 6).

293

294 **Materials and methods**

295 **Animals and genotyping**

296 *Ino80* homozygous floxed (Chakraborty and Magnuson, 2022; Serber et al., 2016)
297 female mice (*Mus musculus*), maintained on an outbred CD1 background, were crossed
298 with *Stra8-Cre*$^{Tg/0}$ males (Sadate-Ngatchou et al., 2008) to produce *Ino80*$^{f/+}$;
299 *Stra8Cre*$^{Tg/0}$ males. Male *Ino80*$^{fl+}$ (*Ino80*^{WT}) and *Ino80*$^{\Delta/f}$*; Stra8Cre*$^{Tg/0}$ (*Ino80*c^{KO})

300 littermates were obtained by crossing *Ino80*$^{f/f}$ females with *Ino80*$^{f/+}$*; Stra8Cre*$^{Tg/0}$ males.
301 Table S1 lists primers used for genotyping. Mice were maintained in an environment
302 with controlled temperature and humidity with 12 h light and 12 h dark cycles and fed *ad*
303 *libitum.* All animal experiments were performed according to the protocol approved by
304 the Institutional Animal Care and Use Committee at the University of North Carolina at
305 Chapel Hill.

306 **RNA isolation and quantitative RT-PCR**

307 Total RNA was isolated from Ino80WT and Ino80cKO spermatocytes using Trizol
308 reagent (Invitrogen) followed by the Direct-zol RNA kit (Zymo). Reverse transcription
309 was performed by the ProtoScript® II reverse transcriptase (NEB) using random
310 primers. Real-time PCR was performed using Sso Fast EvaGreen supermix (Bio-Rad)
311 on a thermocycler (Bio-Rad). Primers used in this study is listed in Table S2.

312 **Immunofluorescence staining**

313 Spermatocyte nuclear spreads were prepared from freshly harvested testes following a
314 published protocol (Wojtasz et al., 2009) with modifications (Biswas et al., 2018). Briefly,
315 single-cell suspensions were prepared from seminiferous tubules. 3μl were added to
316 three volumes of 0.25% NP40 (9ul) on a clean glass slide and incubated for 2 minutes
317 at room temperature. Next, Fixative solution (36ul; 1% paraformaldehyde, 10 mM
318 sodium borate buffer (pH 9.2) was added to the sample, and the slides were incubated
319 in a moist chamber for 2 hours at room temperature. Lastly, slides were dried under a
320 hood, washed with 0.5% Kodak Photo-Flo 200 three times, 1 minute each, and stored at
321 -80˚C.

322 To make cryosections, freshly harvested testes were embedded and frozen in the
323 Optimum Cutting Temperature (OCT) embedding medium. Cryosections (7uM) on glass
324 slides were fixed in freshly made 4% paraformaldehyde solution in PBS for 10 mins at
325 4˚C. Following fixation, samples were washed in PBS 3 times, 5 minutes each, and
326 permeabilized in PBST (PBS + 0.1% Triton-X 100) 3 times for 5 minutes each. Samples
327 were incubated with blocking buffer (10% goat/donkey serum, 2% bovine serum
328 albumin, 0.1% Triton-X 100 in PBS) for 1 hour at RT before incubation with primary
329 antibody (listed in Table. S3) in blocking buffer overnight at 4˚C. The following day,
330 samples were washed 3 times, 5 minutes each with PBST, and incubated with Alexa
331 Fluor-conjugated secondary antibody at room temperature for one hour. Samples were
332 washed once with PBST and counterstained with DAPI, followed by three washes with
333 PBST, 5 minutes each, and mounted in Prolong Gold anti-fade medium (P-36931; Life
334 Technologies).

335 **Isolation of male germ cells**

336 The spermatogenic cells were isolated following a previously published protocol (Chang
337 et al., 2011). Briefly, freshly isolated testes were decapsulated, and seminiferous
338 tubules were digested with collagenase (1mg/ml) in HBSS for 15 minutes at 32˚C. Next,
339 the tubules were precipitated by gravity for 5 mins at room temperature and separated,
340 followed by a second digestion with collagenase (1 mg/ml) and trypsin (0.1%) in HBSS
341 for 15 min at 32˚C. Trypsin was inactivated by adding equal amounts of soybean trypsin
342 inhibitor. The digested product was pipetted and filtered through first 70 uM and then by
343 40uM cell strainers to get spermatocyte suspension. The cells precipitated by
344 centrifugation at 500x*g* for 10 mins, followed by two washes with HBSS. The cells were

345 finally precipitated and either used in a following experiment or frozen at -80˚C for later
346 use.

347 **Nuclear lysate preparation**

348 Nuclear lysate preparations occurred by isolating spermatogenic cells from P21 testes
349 and incubating the cells in a hypotonic buffer (buffer A:10mM HEPES-KOH pH7.9,
350 1.5mM MgCl2, 10mM KCl, 0.1% NP-40, 5mM NaF, 1mM Na3VO4, 1mM PMSF, 1x
351 Protease inhibitor cocktail) using 10-20 times the volume of the precipitated cell volume
352 (PCV). After incubation on ice for 15 minutes, the cells were centrifuged at 1000x*g* for
353 10 minutes at 4˚C. The cells were precipitated and resuspended in buffer A, using twice
354 the PCV, and homogenized with Dounce 'B' pestle 5 times on ice. Cells were
355 precipitated by centrifugation at 1000 x *g* at 4˚C. Precipitated nuclei were washed in
356 buffer A and resuspended in equal volume lysis buffer (Buffer C) (20mM HEPES-KOH
357 pH7.9, 1.5mM MgCl2, 420mM NaCl, 10mM KCl, 25 % glycerol, 0.2mM EDTA, 5mM
358 NaF, 1mM Na3VO4, 1mM PMSF, 1x Protease inhibitor cocktail) for 30 minutes at 4˚C
359 on a nutator. The homogenate was cleared by centrifugation at 12000 x *g* for 10 mins at
360 4˚C and the supernatant saved in a separate tube. The extraction was performed again
361 from the pellet, and the supernatant mixed with the previous one. The lysate was diluted
362 with 2.8 volume of dilution buffer (Buffer D) (20mM HEPES-KOH pH7.9, 20 % glycerol,
363 0.2mM EDTA, 5mM NaF, 1mM Na3VO4, 1mM PMSF, 1x Protease inhibitor cocktail) to
364 reduce the salt concentration and DTT added as necessary to a final concentration of
365 1mM. Some samples were treated with ethidium bromide (50ug/ml) to inhibit DNA-
366 protein interaction (Lai and Herr, 1992) and followed by centrifugation at 12000 x *g* for
367 10 minutes at 4˚C.

368 **Co-Immunoprecipitation**

369 Co-immunoprecipitation was performed using 1-1.5 mg proteins from nuclear extracts
370 from the spermatocytes. The lysate diluted with immunoprecipitation (IP) buffer (20mM
371 HEPES-KOH pH7.9, 0.15mM KCl, 10% glycerol, 0.2mM EDTA, 0.5mM PMSF, 1x
372 Protease inhibitor cocktail) to 1mg/ml concentration. For rabbit antibodies, Protein A
373 conjugated Dynabeads (Invitrogen), and for mouse antibodies, Protein G conjugated
374 Dynabeads (Invitrogen) were used (50ul per sample). Dynabeads were washed in PBS
375 3 times, 1 minute each, followed by incubation in PBS + 0.5% BSA for 10 minutes. Next,
376 the beads were washed in PBS and IP buffer before use. Samples were precleared with
377 dynabeads for 30 minutes at 4˚C, followed by the addition of primary antibody (Table
378 S3) and incubation at 4˚C for 1 hour. Next, dynabeads were added to the samples and
379 incubated overnight at 4˚C. The next day, each sample was washed once in high salt
380 wash buffer (20mM HEPES-KOH pH7.9, 300mM KCl, 10 % glycerol, 0.2mM EDTA, 0.1
381 % Tween-20, 1mM PMSF, Protease inhibitor cocktail), twice in IP wash buffer (20mM
382 HEPES-KOH pH7.9, 150mM KCl, 10 % glycerol, 0.2mM EDTA, 0.1 % Tween-20, 1mM
383 PMSF, Protease inhibitor cocktail), and once in final wash buffer (20mM HEPES-KOH
384 pH7.9, 60mM KCl, 10 % glycerol, 1mM PMSF, 1x Protease inhibitor cocktail). Protein
385 elution was performed using 1.3X Laemmli buffer and incubating at 65˚C for 15 minutes,
386 followed by magnetic removal of Dynabeads. The samples were finally heated at 95˚C
387 for 5 minutes to denature and stored at -20˚C until used.

388 **Western Blotting**

389 Proteins samples were subjected to polyacrylamide gel electrophoresis followed by
390 overnight wet transfer to polyvinylidene difluoride (PVDF) membranes for fluorescence

391 detection. Blots were blocked by Li-COR intercept blocking buffer followed by primary
392 antibody (Table S3) incubation overnight in TBS with 0.1% Tween-20. Fluorescent Li-
393 COR secondary antibodies were used for visualization, and blots were scanned using a
394 Li-COR scanner.

395 **CUT&RUN**

396 Cleavage under targets and release using nuclease (CUT&RUN) was performed using
397 250,000 spermatocytes per sample from *Ino80*^{WT} and *Ino80c*^{KO} testes following a
398 previously published protocol (Meers et al., 2019). Briefly, a single cell suspension of
399 spermatocytes was prepared and immediately washed three times, followed by
400 attachment with concanavalin-A coated beads. These cells were further permeabilized
401 using digitonin and incubated overnight at 4˚C with either IgG or antigen-specific
402 primary antibody (Table S3). The next day, beads were washed twice, followed by
403 protein-A/G-MNase binding in a calcium-free environment. Following two more washes
404 to remove unbound Protein-A/G-MNase, calcium was introduced to start chromatin
405 digestion for 30 mins at 0˚C. Digested chromatin fragments were released for 30 mins
406 at 37˚C. The released chromatin was purified using DNA purification columns (Zymo
407 ChIP DNA Clean & Concentrator). The elute was quantitated, followed by library
408 preparation and qPCR to evaluate enrichment at specific genomic locations with
409 primers listed in Table S2.

410 **Data analysis**

411 ChIP-sequencing data were trimmed as necessary using trimmomatic (Bolger et al.,
412 2014). The reads were aligned to mouse reference genome mm10 using Bowtie2

413 (Langmead and Salzberg, 2012) with sensitive settings. Samtools (Danecek et al.,
414 2021) was used to de-duplicate and merge the alignments. Deeptools (Ramírez et al.,
415 2014) was used to make depth-normalized coverage tracks and metaplots after
416 removing the mm10 blacklisted regions. MACS2 (Zhang et al., 2008)was used to call
417 peaks using the options –extsize set to 147 and –nomodel.

418 RNAseq reads were aligned by Tophat2 (Kim et al., 2013) to mm10, and read counts
419 were obtained by HTseqCount (Anders et al., 2015). DESeq2 (Love et al., 2014) was
420 used with recommended settings to perform differential expression analysis. Plots were
421 prepared by ggplot2 (Wickham, 2016) and chromoMap (Anand and Rodriguez Lopez,
422 2022).

423 ATAC-seq reads were processed by nf-core/atacseq (ver 1.1.0) pipeline (Ewels et al.,
424 2020). Briefly, reads were trimmed by Trim Galore
425 (https://www.bioinformatics.babraham.ac.uk/projects/trim_galore/) and aligned to mouse
426 reference genome mm10 using BWA. Picard (https://broadinstitute.github.io/picard/)
427 was used to mark the duplicates and normalized coverage tracks scaled to 1 million
428 mapped reads were prepared by BEDTools
429 (https://bedtools.readthedocs.io/en/latest/index.html). Differential accessibility analysis
430 was performed by CSAW (Lun and Smyth, 2015) using region-based
431 binned read count followed by TMM normalization using genome-wide background
432 estimation. Genomic annotation of peaks was performed by Homer (Heinz et al., 2010).
433 Plots were created in R using ggplot2 (Wickham, 2016).

434

435 **Statistical analysis**

436 The Wilcoxon rank sum test and the signed-rank test were performed for unpaired and
437 paired observations, respectively, from ChIP-seq or ATAC-seq data. For multiple
438 comparisons, ANOVA was performed, followed by Tukey's *post hoc* test.

439 **Acknowledgment**

440 We thank Magnuson lab members for their input and comments.

441 **Author contribution**

442 P.C. and T.M. conceived the study; P.C. carried out experiments, and data were
443 analyzed and interpreted by P.C. and T.M. Manuscript was written by P.C. and edited
444 by T.M.

445 **Data availability**

446 The sequencing data from RNA-seq, ChIP-seq and ATAC-seq experiments are
447 deposited in the GEO database (Accession number GSE179584 and GSE221682).

448 **Funding**

449 This study was supported by National Institutes of Health grant R01GM101974 (T.M.)
450 and Lalor Foundation Postdoctoral Fellowship (P.C.).

451 **Competing interests**

452 The authors declare no competing or financial interests.

453

454 **References**:

455 **Alatwi, H. E. and Downs, J. A.** (2015). Removal of H2A.Z by INO 80 promotes
456 homologous recombination. *EMBO Rep.* **16**, 986–994.

457 **Allis, C. D. and Jenuwein, T.** (2016). The molecular hallmarks of epigenetic control.
458 *Nat. Rev. Genet. 2016 178* **17**, 487–500.

459 **Anand, L. and Rodriguez Lopez, C. M.** (2022). ChromoMap: an R package for
460 interactive visualization of multi-omics data and annotation of chromosomes. *BMC*
461 *Bioinformatics* **23**, 1–9.

462 **Anders, S., Pyl, P. T. and Huber, W.** (2015). HTSeq-A Python framework to work with
463 high-throughput sequencing data. *Bioinformatics* **31**, 166–169.

464 **Becherel, O. J., Yeo, A. J., Stellati, A., Heng, E. Y. H., Luff, J., Suraweera, A. M.,**
465 **Woods, R., Fleming, J., Carrie, D., McKinney, K., et al.** (2013). Senataxin Plays
466 an Essential Role with DNA Damage Response Proteins in Meiotic Recombination
467 and Gene Silencing. *PLoS Genet.* **9**, e1003435.

468 **Biswas, U., Stevense, M. and Jessberger, R.** (2018). SMC1α Substitutes for Many
469 Meiotic Functions of SMC1β but Cannot Protect Telomeres from Damage. *Curr.*
470 *Biol.* **28**, 249-261.e4.

471 **Bolger, A. M., Lohse, M. and Usadel, B.** (2014). Trimmomatic: A flexible trimmer for
472 Illumina sequence data. *Bioinformatics* **30**, 2114–2120.

473 **Brahma, S., Udugama, M. I., Kim, J., Hada, A., Bhardwaj, S. K., Hailu, S. G., Lee, T.**
474 **H. and Bartholomew, B.** (2017). INO80 exchanges H2A.Z for H2A by

475 translocating on DNA proximal to histone dimers. *Nat. Commun.* **8**, 15616.

476 **Burgoyne, P. S. and Baker, T. G.** (1985). Perinatal oocyte loss in XO mice and its
477 implications for the aetiology of gonadal dysgenesis in XO women . *J. Reprod.*
478 *Fertil.* **75**, 633–645.

479 **Carbajal, A., Gryniuk, I., Castro, R. O. de and Pezza, R. J.** (2022). Efficient
480 enrichment of synchronized mouse spermatocytes suitable for genome-wide
481 analysis. *bioRxiv* 2022.01.11.475957.

482 **Carofiglio, F., Inagaki, A., de Vries, S., Wassenaar, E., Schoenmakers, S.,**
483 **Vermeulen, C., van Cappellen, W. A., Sleddens-Linkels, E., Grootegoed, J. A.,**
484 **te Riele, H. P. J., et al.** (2013). SPO11-Independent DNA Repair Foci and Their
485 Role in Meiotic Silencing. *PLoS Genet.* **9**,.

486 **Chakraborty, P. and Magnuson, T.** (2022). INO80 requires a polycomb subunit to
487 regulate the establishment of poised chromatin in murine spermatocytes. *Dev.*
488 **149**,.

489 **Chang, Y.-F., Lee-Chang, J. S., Panneerdoss, S., MacLean, J. A. and Rao, M. K.**
490 (2011). Isolation of Sertoli, Leydig, and spermatogenic cells from the mouse testis.
491 *Biotechniques* **51**, 341–344.

492 **Danecek, P., Bonfield, J. K., Liddle, J., Marshall, J., Ohan, V., Pollard, M. O.,**
493 **Whitwham, A., Keane, T., McCarthy, S. A., Davies, R. M., et al.** (2021). Twelve
494 years of SAMtools and BCFtools. *Gigascience* **10**, 1–4.

495 **Dowdle, J. A., Mehta, M., Kass, E. M., Vuong, B. Q., Inagaki, A., Egli, D., Jasin, M.**

496 **and Keeney, S.** (2013). Mouse BAZ1A (ACF1) Is Dispensable for Double-Strand
497 Break Repair but Is Essential for Averting Improper Gene Expression during
498 Spermatogenesis. *PLoS Genet.* **9**, e1003945.

499 **Ewels, P. A., Peltzer, A., Fillinger, S., Patel, H., Alneberg, J., Wilm, A., Garcia, M.**
500 **U., Di Tommaso, P. and Nahnsen, S.** (2020). The nf-core framework for
501 community-curated bioinformatics pipelines. *Nat. Biotechnol.* **38**, 276–278.

502 **Fayer, S., Yu, Q., Kim, J., Moussette, S., Camerini-Otero, R. D. and Naumova, A. K.**
503 (2016). Robertsonian translocations modify genomic distribution of γH2AFX and
504 H3.3 in mouse germ cells. *Mamm. Genome* **27**, 225–236.

505 **Fedoriw, A. M., Menon, D., Kim, Y., Mu, W. and Magnuson, T.** (2015). Key mediators
506 of somatic ATR signaling localize to unpaired chromosomes in spermatocytes. *Dev.*
507 **142**, 2972–2980.

508 **Fernandez-Capetillo, O., Mahadevaiah, S. K., Celeste, A., Romanienko, P. J.,**
509 **Camerini-Otero, R. D., Bonner, W. M., Manova, K., Burgoyne, P. and**
510 **Nussenzweig, A.** (2003). H2AX is required for chromatin remodeling and
511 inactivation of sex chromosomes in male mouse meiosis. *Dev. Cell* **4**, 497–508.

512 **Handel, M. A. and Schimenti, J. C.** (2010). Genetics of mammalian meiosis:
513 Regulation, dynamics and impact on fertility. *Nat. Rev. Genet.* **11**, 124–136.

514 **Heinz, S., Benner, C., Spann, N., Bertolino, E., Lin, Y. C., Laslo, P., Cheng, J. X.,**
515 **Murre, C., Singh, H. and Glass, C. K.** (2010). Simple Combinations of Lineage-
516 Determining Transcription Factors Prime cis-Regulatory Elements Required for
517 Macrophage and B Cell Identities. *Mol. Cell* **38**, 576–589.

518 **Hirota, T., Blakeley, P., Sangrithi, M. N., Mahadevaiah, S. K., Encheva, V., Snijders,**
519 **A. P., Ellnati, E., Ojarikre, O. A., de Rooij, D. G., Niakan, K. K., et al.** (2018).
520 SETDB1 Links the Meiotic DNA Damage Response to Sex Chromosome Silencing
521 in Mice. *Dev. Cell* **47**, 645-659.e6.

522 **Ichijima, Y., Ichijima, M., Lou, Z., Nussenzweig, A., Daniel Camerini-Otero, R.,**
523 **Chen, J., Andreassen, P. R. and Namekawa, S. H.** (2011a). MDC1 directs
524 chromosome-wide silencing of the sex chromosomes in male germ cells. *Genes*
525 *Dev.* **25**, 959–971.

526 **Ichijima, Y., Ichijima, M., Lou, Z., Nussenzweig, A., Daniel Camerini-Otero, R.,**
527 **Chen, J., Andreassen, P. R. and Namekawa, S. H.** (2011b). MDC1 directs
528 chromosome-wide silencing of the sex chromosomes in male germ cells. *Genes*
529 *Dev.* **25**, 959–971.

530 **Ichijima, Y., Sin, H. S. and Namekawa, S. H.** (2012). Sex chromosome inactivation in
531 germ cells: Emerging roles of DNA damage response pathways. *Cell. Mol. Life Sci.*
532 **69**, 2559–2572.

533 **Imai, Y., Biot, M., Clément, J. A. J., Teragaki, M., Urbach, S., Robert, T., Baudat, F.,**
534 **Grey, C. and de Massy, B.** (2020). Prdm9 activity depends on hells and promotes
535 local 5-hydroxymethylcytosine enrichment. *Elife* **9**, e57117.

536 **Kim, Y., Fedoriw, A. M. and Magnuson, T.** (2012). An essential role for a mammalian
537 SWI/SNF chromatin-remodeling complex during male meiosis. *Development* **139**,
538 1133–1140.

539 **Kim, D., Pertea, G., Trapnell, C., Pimentel, H., Kelley, R. and Salzberg, S. L.** (2013).

540 TopHat2: Accurate alignment of transcriptomes in the presence of insertions,
541 deletions and gene fusions. *Genome Biol.* **14**, R36.

542 **Lai, J. S. and Herr, W.** (1992). Ethidium bromide provides a simple tool for identifying
543 genuine DNA- independent protein associations. *Proc. Natl. Acad. Sci. U. S. A.* **89**,
544 6958–6962.

545 **Langmead, B. and Salzberg, S. L.** (2012). Fast gapped-read alignment with Bowtie 2.
546 *Nat. Methods* **9**, 357–359.

547 **Li, W., Wu, J., Kim, S. Y., Zhao, M., Hearn, S. A., Zhang, M. Q., Meistrich, M. L. and**
548 **Mills, A. A.** (2014). Chd5 orchestrates chromatin remodelling during sperm
549 development. *Nat. Commun.* **5**, 3812.

550 **Love, M. I., Huber, W. and Anders, S.** (2014). Moderated estimation of fold change
551 and dispersion for RNA-seq data with DESeq2. *Genome Biol.* **15**, 550.

552 **Luijsterburg, M. S. and Van Attikum, H.** (2011). Chromatin and the DNA damage
553 response: The cancer connection. *Mol. Oncol.* **5**, 349–367.

554 **Lun, A. T. L. and Smyth, G. K.** (2015). Csaw: A Bioconductor package for differential
555 binding analysis of ChIP-seq data using sliding windows. *Nucleic Acids Res.* **44**,
556 e45.

557 **Maezawa, S., Yukawa, M., Alavattam, K. G., Barski, A. and Namekawa, S. H.** (2018).
558 Dynamic reorganization of open chromatin underlies diverse transcriptomes during
559 spermatogenesis. *Nucleic Acids Res.* **46**, 593–608.

560 **Meers, M. P., Bryson, T. D., Henikoff, J. G. and Henikoff, S.** (2019). Improved

561 CUT&RUN chromatin profiling tools. *Elife* **8**, e46314.

562 **Morrison, A. J.** (2017). Genome maintenance functions of the INO80 chromatin
563 remodeller. *Philos. Trans. R. Soc. B Biol. Sci.* **372**, 20160289.

564 **Morrison, A. J., Highland, J., Krogan, N. J., Arbel-Eden, A., Greenblatt, J. F.,**
565 **Haber, J. E. and Shen, X.** (2004). INO80 and γ-H2AX Interaction Links ATP-
566 Dependent Chromatin Remodeling to DNA Damage Repair. *Cell* **119**, 767–775.

567 **Papamichos-Chronakis, M., Watanabe, S., Rando, O. J. and Peterson, C. L.** (2011).
568 Global regulation of H2A.Z localization by the INO80 chromatin-remodeling enzyme
569 is essential for genome integrity. *Cell* **144**, 200–213.

570 **Poli, J., Gerhold, C. B., Tosi, A., Hustedt, N., Seeber, A., Sack, R., Herzog, F.,**
571 **Pasero, P., Shimada, K., Hopfner, K. P., et al.** (2016). Mec1, INO80, and the
572 PAF1 complex cooperate to limit transcription replication conflicts through RNAPII
573 removal during replication stress. *Genes Dev.* **30**, 337–354.

574 **Poli, J., Gasser, S. M. and Papamichos-Chronakis, M.** (2017). The INO80 remodeller
575 in transcription, replication and repair. *Philos. Trans. R. Soc. B Biol. Sci.* **372**,
576 20160290.

577 **Price, B. D., D'Andrea, A. D., Ahel, D., Horejsí, Z., Wiechens, N., Polo, S. E.,**
578 **Garcia-Wilson, E., Ahel, I., Flynn, H., Skehel, M., et al.** (2013). Chromatin
579 remodeling at DNA double-strand breaks. *Cell* **152**, 1344–54.

580 **Ramírez, F., Dündar, F., Diehl, S., Grüning, B. A. and Manke, T.** (2014). DeepTools:
581 A flexible platform for exploring deep-sequencing data. *Nucleic Acids Res.* **42**,

582 W187–W191.

583 **Royo, H., Prosser, H., Ruzankina, Y., Mahadevaiah, S. K., Cloutier, J. M.,**
584 **Baumann, M., Fukuda, T., Höög, C., Tóth, A., de Rooij, D. G., et al.** (2013). ATR
585 acts stage specifically to regulate multiple aspects of mammalian meiotic silencing.
586 *Genes Dev.* **27**, 1484–1494.

587 **Sadate-Ngatchou, P. I., Payne, C. J., Dearth, A. T. and Braun, R. E.** (2008). Cre
588 recombinase activity specific to post natal, premeiotic male germ cells in transgenic
589 mice. *Genesis* **46**, 738–742.

590 **Schoenmakers, S., Wassenaar, E., van Cappellen, W. A., Derijck, A. A., de Boer,**
591 **P., Laven, J. S. E., Grootegoed, J. A. and Baarends, W. M.** (2008). Increased
592 frequency of asynapsis and associated meiotic silencing of heterologous chromatin
593 in the presence of irradiation-induced extra DNA double strand breaks. *Dev. Biol.*
594 **317**, 270–281.

595 **Serber, D. W., Runge, J. S., Menon, D. U. and Magnuson, T.** (2016). The mouse
596 INO80 chromatin-remodeling complex is an essential meiotic factor for
597 spermatogenesis. *Biol. Reprod.* **94**, 1–9.

598 **Solari, A. J.** (1964). The morphology and ultrastructure of the sex vesicle in the mouse.
599 *Exp. Cell Res.* **36**, 160–168.

600 **Spruce, C., Dlamini, S., Ananda, G., Bronkema, N., Tian, H., Paigen, K., Carter, G.**
601 **W. and Baker, C. L.** (2020). HELLS and PRDM9 form a pioneer complex to open
602 chromatin at meiotic recombination hot spots. *Genes Dev.* **34**, 398–412.

603 **Stewart, G. S., Wang, B., Bigneli, C. R., Taylor, A. M. R. and Elledge, S. J.** (2003).
604 MDC1 is a mediator of the mammalian DNA damage checkpoint. *Nature* **421**, 961–
605 966.

606 **Stucki, M., Clapperton, J. A., Mohammad, D., Yaffe, M. B., Smerdon, S. J. and**
607 **Jackson, S. P.** (2005). MDC1 directly binds phosphorylated histone H2AX to
608 regulate cellular responses to DNA double-strand breaks. *Cell* **123**, 1213–1226.

609 **Turner, J. M. A.** (2015). Meiotic Silencing in Mammals. *Annu. Rev. Genet.* **49**, 395–
610 412.

611 **Turner, J. M. A., Aprelikova, O., Xu, X., Wang, R., Kim, S., Chandramouli, G. V. R.,**
612 **Barrett, J. C., Burgoyne, P. S. and Deng, C. X.** (2004). BRCA1, histone H2AX
613 phosphorylation, and male meiotic sex chromosome inactivation. *Curr. Biol.* **14**,
614 2135–2142.

615 **Wang, J., Gu, H., Lin, H. and Chi, T.** (2012). Essential roles of the chromatin
616 remodeling factor BRG1 in spermatogenesis in mice. *Biol. Reprod.* **86**, 186.

617 **Wang, L., Du, Y., Ward, J. M., Shimbo, T., Lackford, B., Zheng, X., Miao, Y. L.,**
618 **Zhou, B., Han, L., Fargo, D. C., et al.** (2014). INO80 facilitates pluripotency gene
619 activation in embryonic stem cell self-renewal, reprogramming, and blastocyst
620 development. *Cell Stem Cell* **14**, 575–591.

621 **Wickham, H.** (2016). *ggplot2: Elegant Graphics for Data Analysis*. Springer-Verlag New
622 York.

623 **Wojtasz, L., Daniel, K., Roig, I., Bolcun-Filas, E., Xu, H., Boonsanay, V., Eckmann,**

C. R., Cooke, H. J., Jasin, M., Keeney, S., et al. (2009). Mouse HORMAD1 and HORMAD2, two conserved meiotic chromosomal proteins, are depleted from synapsed chromosome axes with the help of TRIP13 AAA-ATPase. *PLoS Genet.* **5**, e1000702.

Yan, W. and McCarrey, J. R. (2009). Sex chromosome inactivation in the male. *Epigenetics* **4**, 452–456.

Yeo, A. J., Becherel, O. J., Luff, J. E., Graham, M. E., Richard, D. and Lavin, M. F. (2015). Senataxin controls meiotic silencing through ATR activation and chromatin remodeling. *Cell Discov.* **1**, 15025.

Yu, H., Wang, J., Lackford, B., Bennett, B., Li, J. and Hu, G. (2021). INO80 promotes H2A.Z occupancy to regulate cell fate transition in pluripotent stem cells. *Nucleic Acids Res.* **49**, 6739–6755.

Zhang, Y., Liu, T., Meyer, C. A., Eeckhoute, J., Johnson, D. S., Bernstein, B. E., Nussbaum, C., Myers, R. M., Brown, M., Li, W., et al. (2008). Model-based analysis of ChIP-Seq (MACS). *Genome Biol.* **9**, r137.

Zhou, B., Wang, L., Zhang, S., Bennett, B. D., He, F., Zhang, Y., Xiong, C., Han, L., Diao, L., Li, P., et al. (2016). INO80 governs superenhancer-mediated oncogenic transcription and tumor growth in melanoma. *Genes Dev.* **30**, 1440–1453.

643 **Figure legends**

644 **Figure 1: INO80 localization in the germ cells**. (A,B) INO80 immunolocalization in the
645 pachytene spermatocyte spreads (A) and the seminiferous tubule of the testis (B).
646 SCP3 staining indicates the stage of the meiotic spermatocyte. Magenta: SCP3, Green:
647 INO80, Blue: DAPI. Arrowhead: Sex chromosomes. Scale bar = 10μM. C; Enrichment
648 of INO80 obtained by ChIP-seq on the XY chromosomes during zygonema at postnatal
649 day 18 (P18), where most cells are in the pachytene stage. Blue: P18, Red: Zygonema.

650

651 **Figure 2**: **INO80 required for transcriptional silencing of sex chromosomes during**
652 **meiotic prophase.** (A) Boxplots showing mean differential gene expression from each
653 chromosome in response to *Ino80* deletion in spermatocytes. The yellow dotted line
654 indicates mean Log_2FoldChange = 0. Chr: Chromosome. (B) Quantitative RT-PCR
655 analysis of representative sex-linked gene expression levels normalized to *Rplp2* in
656 either *Ino80*WT or *Ino80*cKO testes. *; $p<0.05$. (C) Location of the differentially
657 regulated genes along the length of three representative autosomes and the sex
658 chromosomes. Dots above each chromosome indicate the fold change of individual
659 genes. Upregulated and downregulated genes are indicated by red and blue,
660 respectively. (D) Immunolocalization of SCP3 (magenta) and RNA Polymerase II
661 (pSer2) (green) in spermatocytes either from *Ino80*WT or *Ino80*cKO (Scale bar = 10μM)
662 showing aberrant localization RNA Polymerase II (pSer2) in *Ino80*cKO spermatocytes
663 that are indicative of incomplete sex-chromosome silencing. White arrowhead; sex
664 chromosome. The white circle denotes an approximate area of the sex body.

665

666 **Figure 3: DNA damage repair factor recruitment at the sex chromosomes**
667 **facilitated by INO80.** (A,B) Immunolocalization of SCP3 (magenta) and either ATR
668 (green) (A) or pCHK1 (S345) (green) (B) in spermatocytes from *Ino80*WT or *Ino80*cKO.
669 DAPI shown in blue. Scale bar = 10μM. White arrowhead; sex-chromosome. (C)
670 Immunolocalization of SCP3 (magenta) and MDC1 (green) in spermatocytes from
671 *Ino80*WT or *Ino80*cKO. Scale bar = 10μM. White arrowhead; sex-chromosome. DAPI
672 showed in blue. Scale bar = 10μM. (D) Fluorescent intensity measurement of MDC1
673 signal at the sex chromosomes from either *Ino80*WT or *Ino80*cKO pachytene
674 spermatocytes. *; $p<0.05$ (E) Immunoblot images demonstrating the interaction of
675 INO80 with ATR and MDC1 by the presence of MDC1 and ATR in INO80
676 immunoprecipitated *Ino80*WT spermatocyte homogenates and INO80 when
677 immunoprecipitated with MDC1 from *Ino80*WT spermatocyte homogenate.

678

679 **Figure 4: Aberrant γH2A.X localization in *Ino80cKO* spermatocytes**.
680 Immunolocalization of SCP3 (magenta) and γH2A.X (green) in pachytene
681 spermatocytes from *Ino80*WT or *Ino80*cKO (Scale bar = 10μM). DAPI is shown in blue.
682 Scale bar = 10μM. White arrowhead; sex-chromosome.

683 **Figure 5: INO80 regulates chromatin accessibility in spermatocyte sex**
684 **chromosomes.** (A) Dot plot showing the relative changes in accessibility on each
685 chromosome at P18 pachytene spermatocytes compared to P12 zygotene
686 spermatocytes. Red dot: FDR < 0.05; Black dot: FDR > 0.05. (B) Genomic annotation of

687 the differentially accessible regions from (FDR < 0.05) as shown in (A). (C) Dot plot
688 showing relative changes in chromatin accessibility on each accessible site in each
689 chromosome due to *Ino80* deletion at P18. Red dot: FDR < 0.05; Black dot: FDR > 0.05.
690 (D) Genomic annotation of the differentially accessible regions from (FDR < 0.05) as
691 shown in (C). (D); Genomic annotation of the differentially accessible regions due to
692 *Ino80* deletion. (E) Boxplot showing the mean change in ATAC-signal (chromatin
693 accessibility) at all the γH2A.X marked DSB sites (Fayer et al., 2016) between *Ino80*WT
694 and *Ino80*cKO in P18 spermatocytes. *; p<0.05.

695 **Figure 6**: **Schematic illustration of INO80-mediated regulation of meiotic sex-**
696 **chromosome silencing**. INO80 facilitates MDC1 recruitment at the DSB sites and
697 regulates chromatin accessibility at these regions. MDC1 recruitment allows ATR-
698 mediated amplification of γH2A.X at the chromatin loops. *Ino80*-deletion results in
699 decreased chromatin accessibility and a lack of MDC1 recruitment, which fails to initiate
700 ATR-mediated amplification of γH2A.X.

701 **Figure S1:** INO80 binding at the DSB sites. Genomic tracks illustrating INO80 binding
702 at the DSB sites marked by γH2A.X (Fayer et al., 2016) in P18 (Chakraborty and
703 Magnuson, 2022) and zygotene (Carbajal et al., 2022) spermatocytes. Each separate
704 genomic location is denoted by alternating background coloring. IG-Up; Intergenic-
705 Upstream.

706 **Figure S2:** INO80 facilitates MDC1 recruitment and expression. (A) Bar plot showing
707 input normalized enrichment of MDC1 binding determined by CUT&RUN followed by
708 qPCR analysis. Each pair of bars represent enrichment in either *Ino80*WT (blue) or
709 *Ino80*cKO (orange) spermatocytes. Each location in the X-axis represents sex-linked

710 DSB regions marked by γH2A.X (Fayer et al., 2016). The negative control region is GD.
711 IntGen = Intergenic region, Int=Intron. (B) Boxplot showing the normalized count of
712 *Mdc1* transcripts from *Ino80*WT and *Ino80*cKO spermatocytes. (C) Immunoblot showing
713 MDC1 (top) and α-Actin (bottom) expression from *Ino80*WT and *Ino80*cKO
714 spermatocytes on P18. (D) Genomic tracks illustrated the enrichment of INO80,
715 H3K27me3, and H3K4me3 at the *Mdc1* promoter-proximal area. (E) Immunoblot
716 images demonstrate the interaction between INO80 with ATR and MDC1 by the
717 presence of INO80 in both ATR and MDC1 immunoprecipitated samples. The top panel
718 shows two brightness and contrast levels from the same blot to visualize MDC1 in input
719 and immunoprecipitation samples. Spliced sections in the bottom panel are part of the
720 same blot.

721 **Figure S3**: Metaplot illustrating changes in H2A.Z (A-B), H3K4me3 (C), and
722 H3K27me3 (D) occupancy at either INO80 binding sites (A) or promoter/TSS regions
723 (B-D) in sex chromosomes.

724 **Figure S4**: (A) Metaplot illustrating chromatin accessibility at the promoter/TSS regions
725 of autosomes and sex chromosomes in either P12 *Ino80*WT or P18 *Ino80*WT and
726 *Ino80*cKO spermatocytes. (B) Comparison of ATAC peaks during the transition from
727 P12 spermatocyte to P18 spermatocyte and in P18 *Ino80*WT vs. *Ino80*cKO
728 spermatocytes. (C) Genomic annotation of ATAC-peaks in P12 and P18 spermatocytes,
729 as well as the peaks that were de novo generated during pachynema transition during
730 P18 and lost due to *Ino80* deletion.

731

732

733

734

735 Table S1: Genotyping primers used in this study.

Allele	**Sequence**
Ino80 floxed forward	5'-GATACTTCTGCCTCCACACTTC-3'
Ino80 floxed reverse	5'-CTGGCACCTTTCCAGTCTTT-3'
Ino80 excised forward	5'-TGTGTAGCAACCTACAGCTA-3'
Ino80 excised reverse	5'-GTTGCTGTGTCTTTGCTTTG-3'
Stra8Cre forward	5'-GTGCAAGCTGAACAACAGGA-3'
Stra8Cre reverse	5'-AGGGACACAGCATTGGAGTC-3'

736

737

738

739

740

741

742

743

744

745

746

747

748

749

750

751

752

753

754

755

756 Table S2: Quantitative PCR primers used in this study.

Region/Gene	**Sequence**
Ccnb3 Forward	5'-GCTCACCTCAAGCCCATTAT-3'
Ccnb3 Reverse	5'-TTGACTGGTGGCTTCTCTTTAG-3'
Nxt2 Forward	5'-GTAGAGCTGCCGAGGAATTT-3'
Nxt2 Reverse	5'-TCCAGATTAGAGTGGCTTTGTC-3'
Eda2r Forward	5'-CCAGTTGAGCTTAGTGAAGGTAG-3'
Eda2r Reverse	5'-AGGAAGGCCAGAGCAAATAC -3'
Abcd1 Forward	5'-TGGATGGACGACTTCGAAAC-3'
Abcd1 Reverse	5'-GGCTTGGTCAGGTTGGAATA-3'
Usp11 Forward	5'-GCTCGTTCAGCACAGTGATA-3'
Usp11 Reverse	5'-TCCTGAGGCTCTACCAGAAA-3'
Rplp2 Forward	5'-CCTAGCGCCAAAGACATCAA-3'
Rplp2 Reverse	5'-GACCTTGTTGAGCCGATCAT-3'
GD Forward	5'-TGCCTTAGGGAGAGAGTGATAG-3'
GD Reverse	5'-TCCACACGTCCAGTGATTTG-3'
IntGen 1 Forward	5'-AGCTTGAACAGAGAGTCAACAG-3'
IntGen 1 Reverse	5'-CAAGGCTCATCATGAATGGAATG-3'
IntGen 2 Forward	5'-GAAGGAGGGAATGGGATTGT-3'
IntGen 2 Reverse	5'-GAGTTATGGCCTCGAAGTAGTC-3'
Prrg1 int3 Forward	5'-CATGGATGCGAGGCCATTA-3'
Prrg1 int3 Reverse	5'-ACACTTCAGAATGAGCAAGGAG-3'
Atg4a int9 Forward	5'-GGCAGAGGCATAGGTGAAA-3'
Atg4a int9 Reverse	5'-TGCTCCTCTGCCACAATTC-3'

Shroom4 ex4 Forward	5'-TCACGGTCCTCAGCATAGT-3'
Shroom4 ex4 Reverse	5'-GGCTGCCTTCCTGGATTT-3'
IntGen 3 Forward	5'-GTAGGTCATGGGTTCCAACT-3'
IntGen 3 Reverse	5'-AGTAACCATCTGGTGCTCTG-3'

757

758 Table S3: Primary antibodies used in this study.

Primary antibody	**Source**	**Amount/Dilution**
Rabbit anti-INO80	Abcam (ab105451)	ChIP-seq (10µg) WB (1:2000) IF (1:700)
Rabbit anti-INO80	Novus Biologicals (NBP1-78758)	IP (10 µg) IF (1:500)
Rabbit anti-ATR	Abcam (ab2905)	IP (10 µg)
Rabbit anti-ATR	Millipore (09-070)	WB (1:1000)
Goat anti-ATR	Santa Cruz (sc-1887)	IF (1:50)
Rabbit anti phospho-CHK1(Ser345)	Cell signaling (2348)	IF (1:200)
Mouse anti-MDC1	Novus Biologicals (NBP2-12890)	WB (1:1000) IF (1:200) CUT&RUN (1:200)
Mouse anti-alpha-Actin	Santa Cruz (sc-32251)	WB (1:2000)
Mouse anti-SYCP3	Abcam (ab97672)	IF (1:1000)
Rabbit anti-SYCP3	Novus Biologicals (NB300-231)	IF (1:200)
Goat anti-phospho RNA Polymerase II (Ser2)	Active Motif (61084)	IF: (1:200)

Mouse anti-γH2A.X	Millipore (05-636)	IF (1:1500)

759

760

761

Chakraborty_Figure. 1

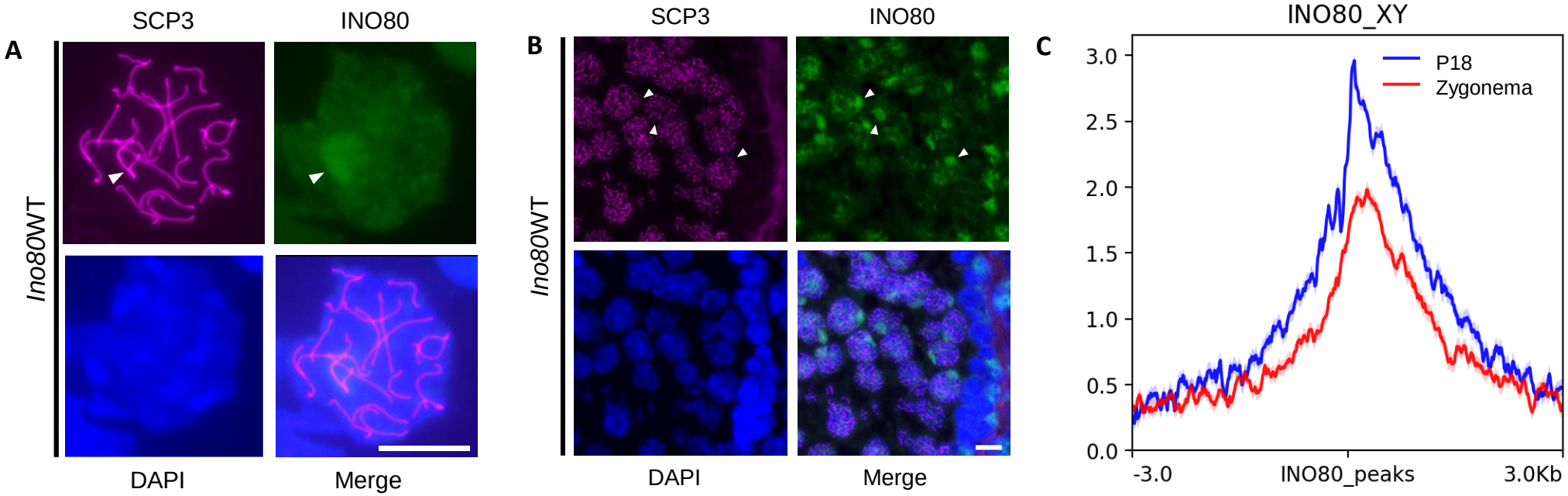

Chakraborty_Figure. S1

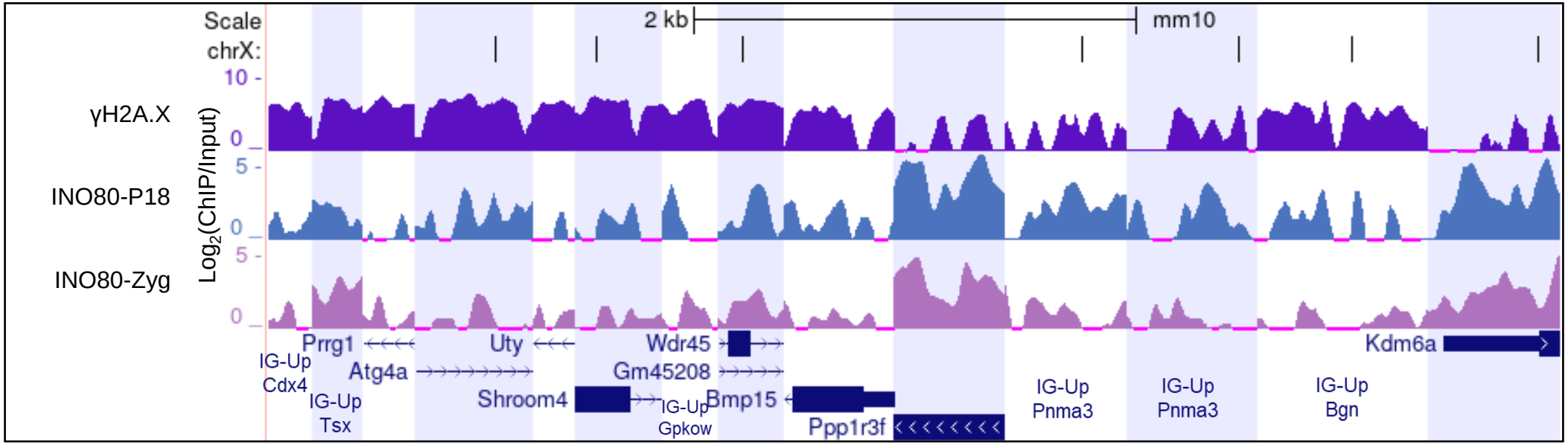

Chakraborty_Figure. 2

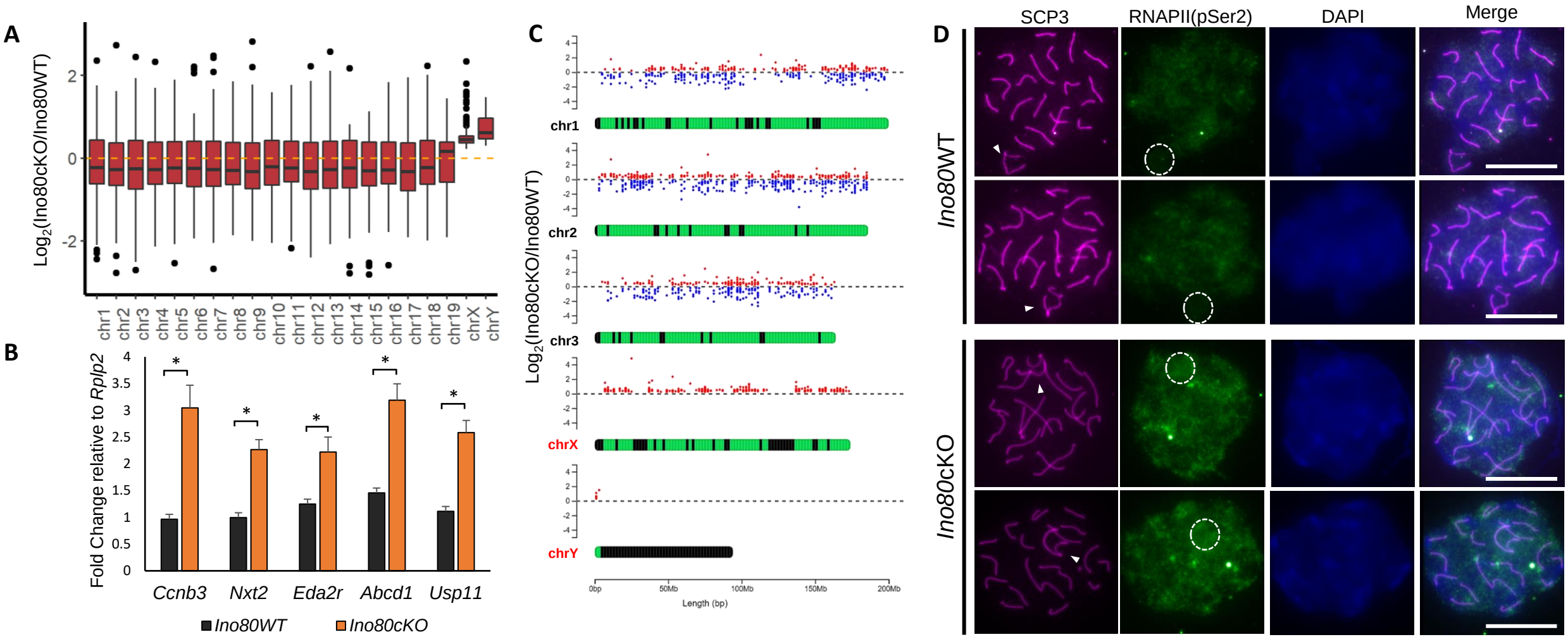

Chakraborty_Figure. 3

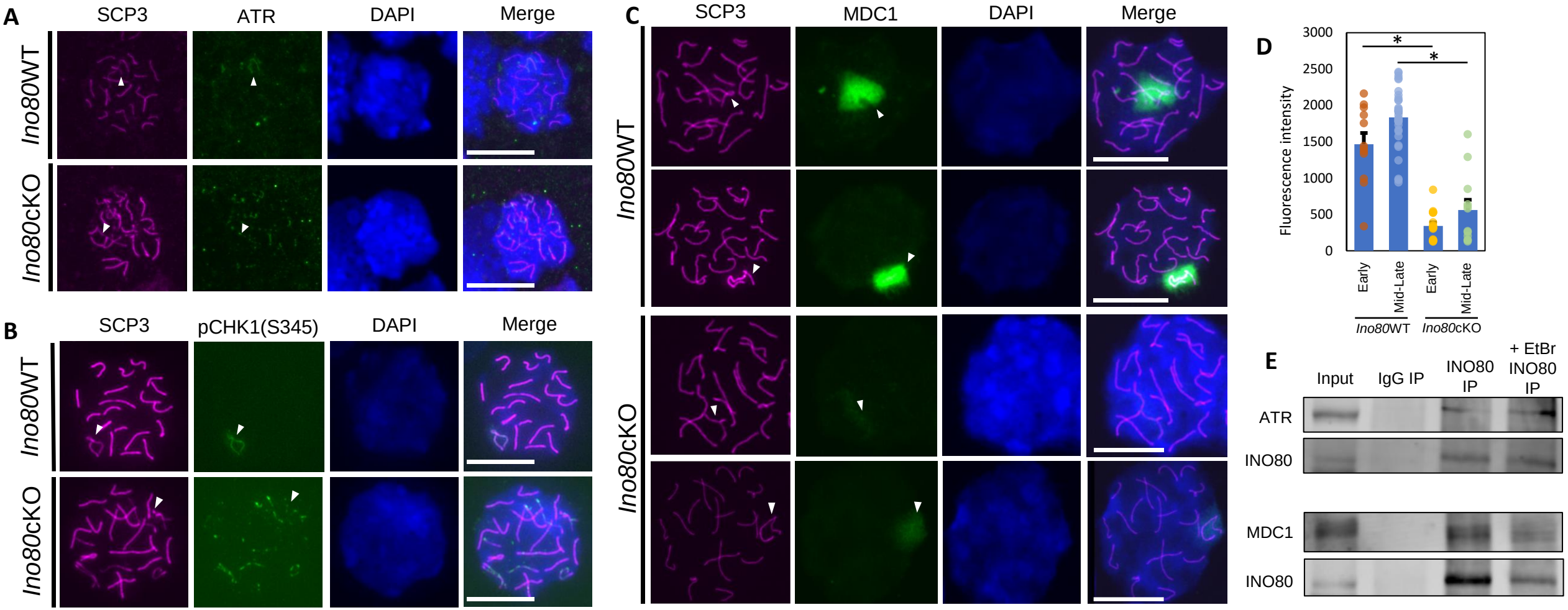

Chakraborty_Figure. S2

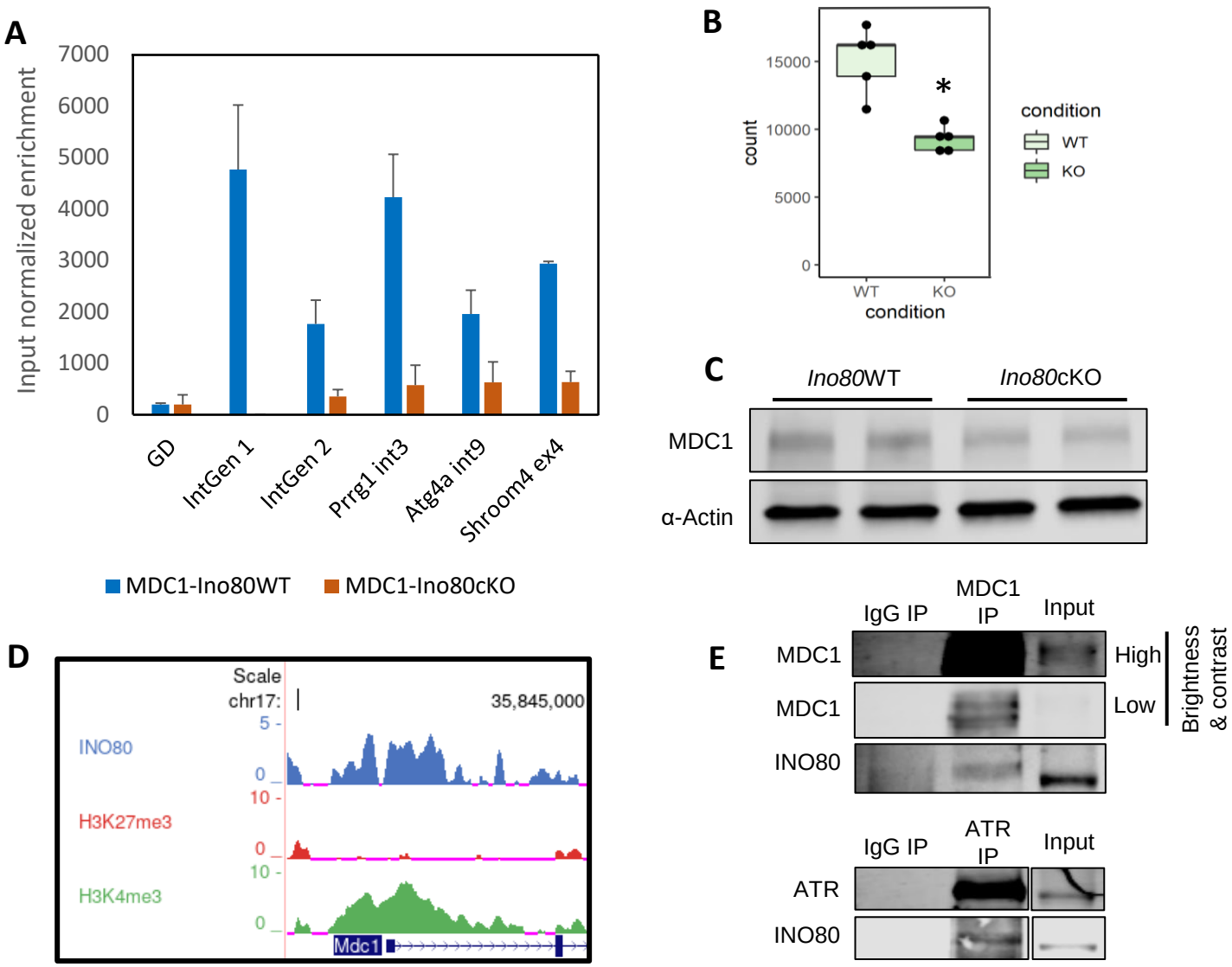

Chakraborty_Figure. 4

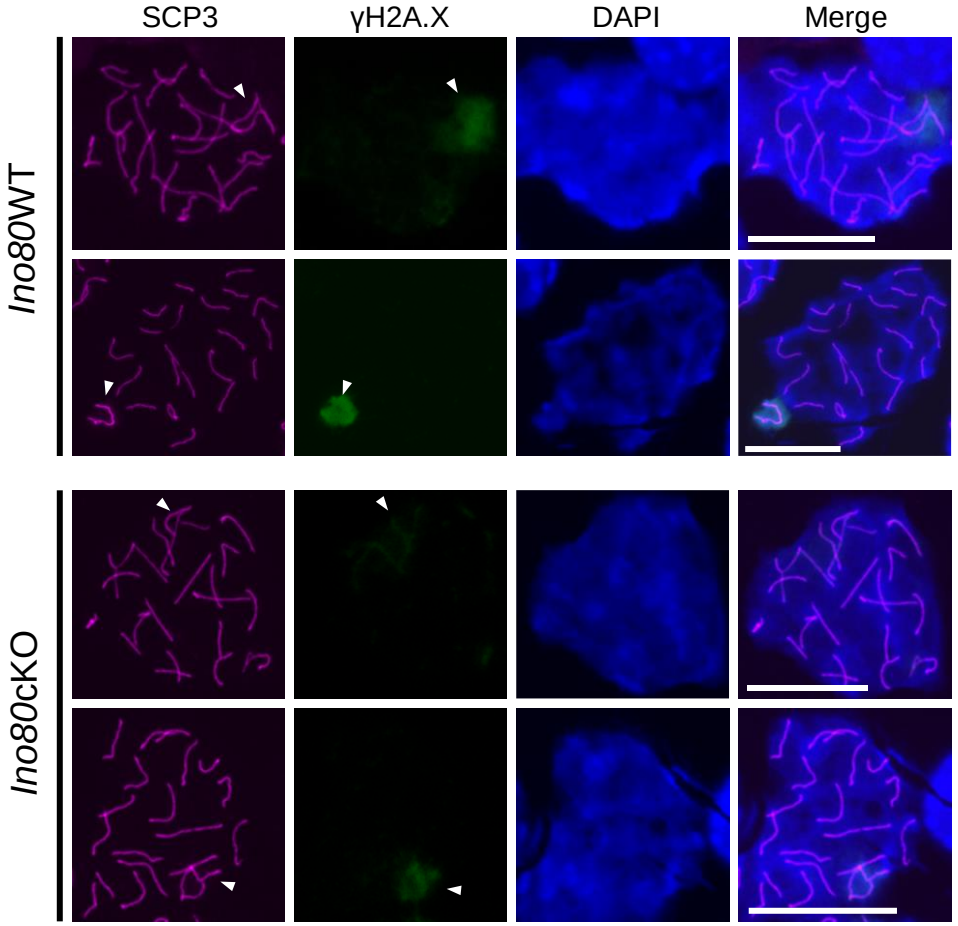

Chakraborty_Figure. S3

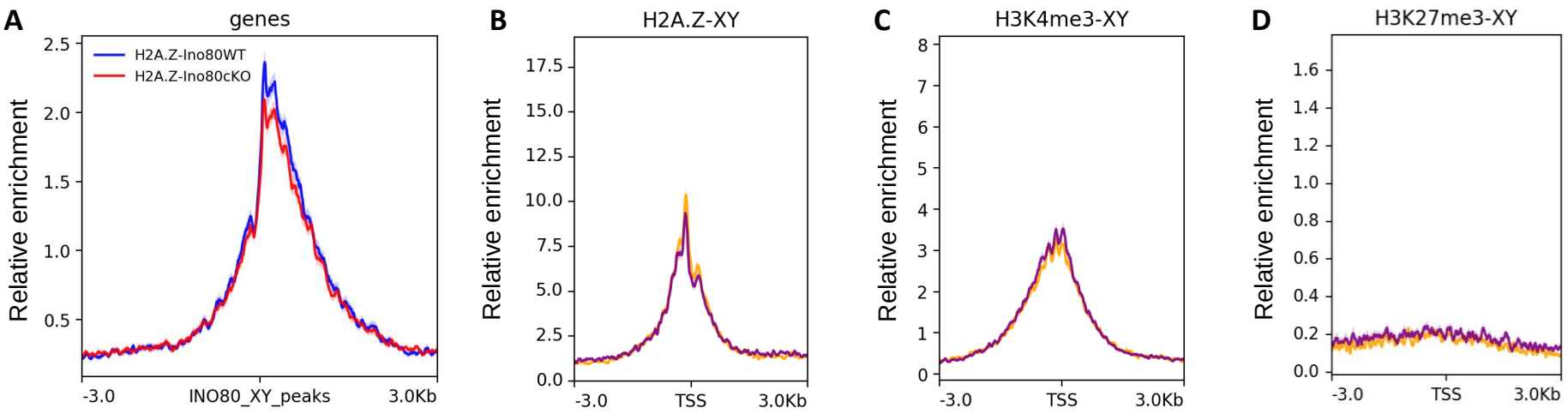

Chakraborty_Figure. S4

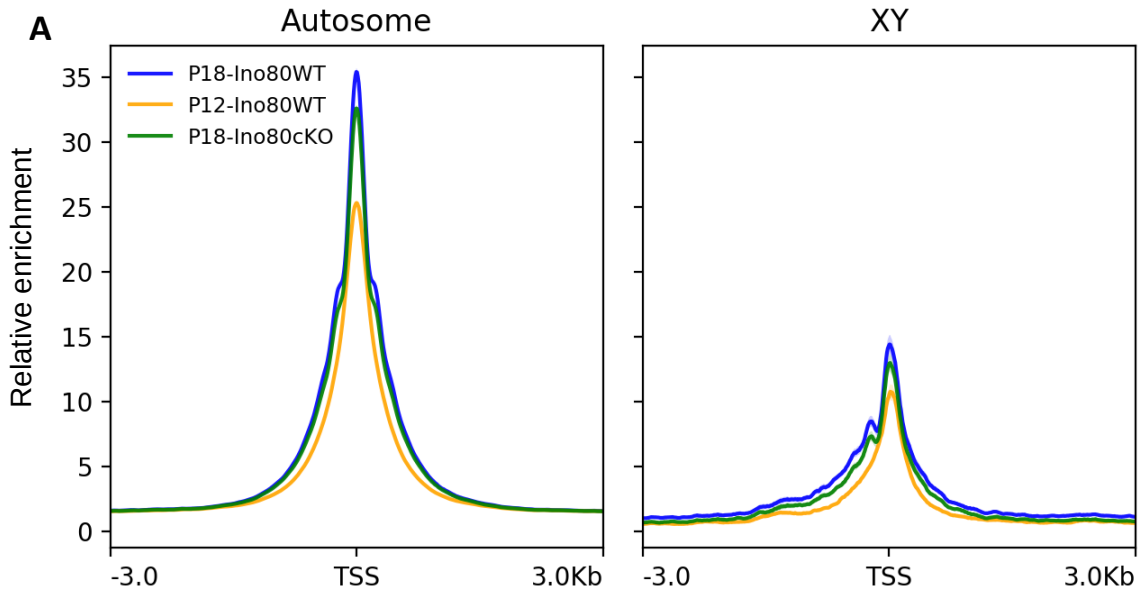

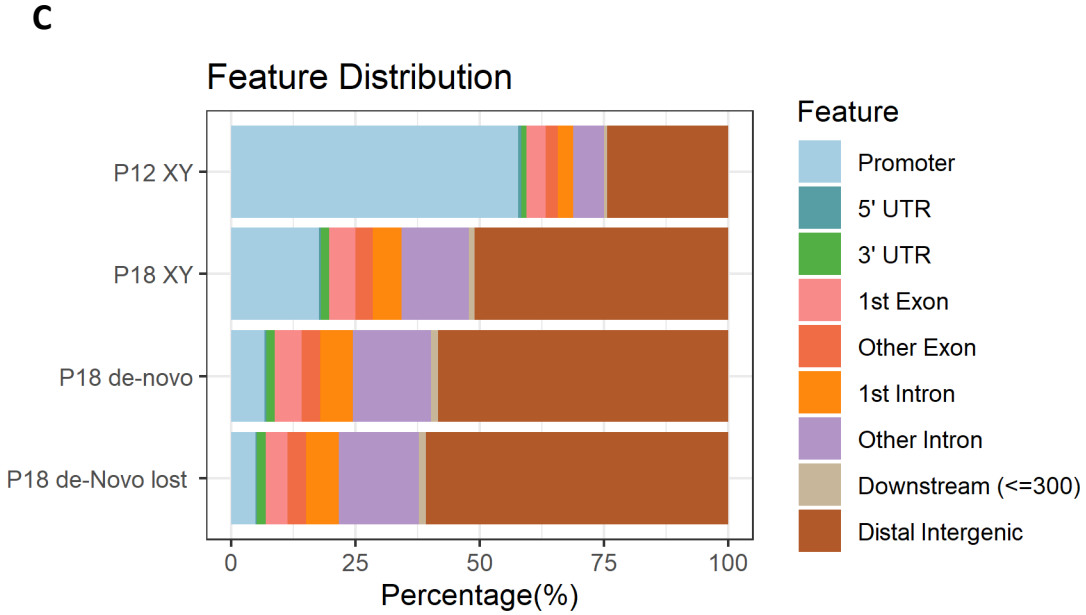

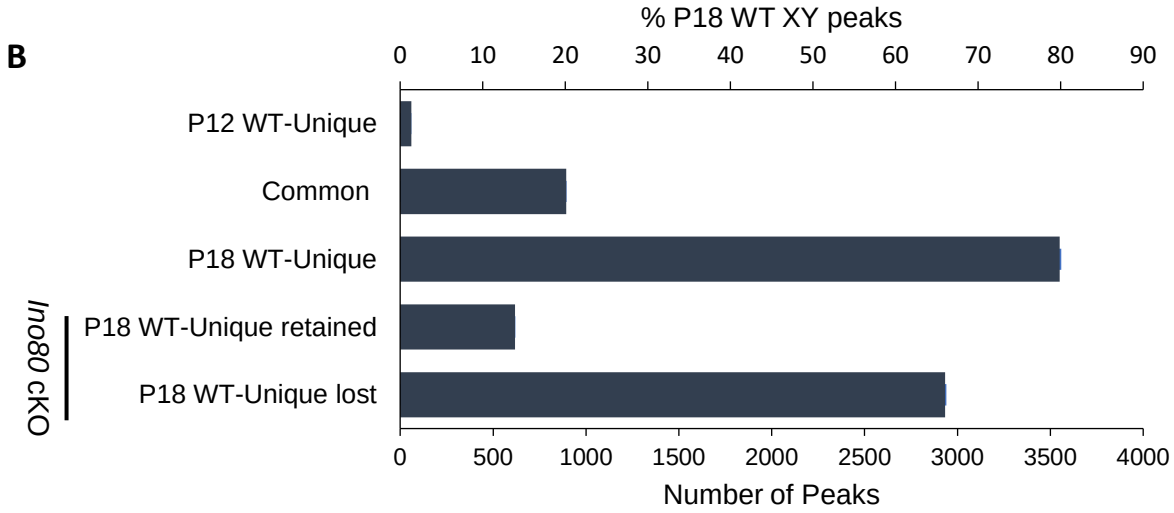

Chakraborty_Figure. 5

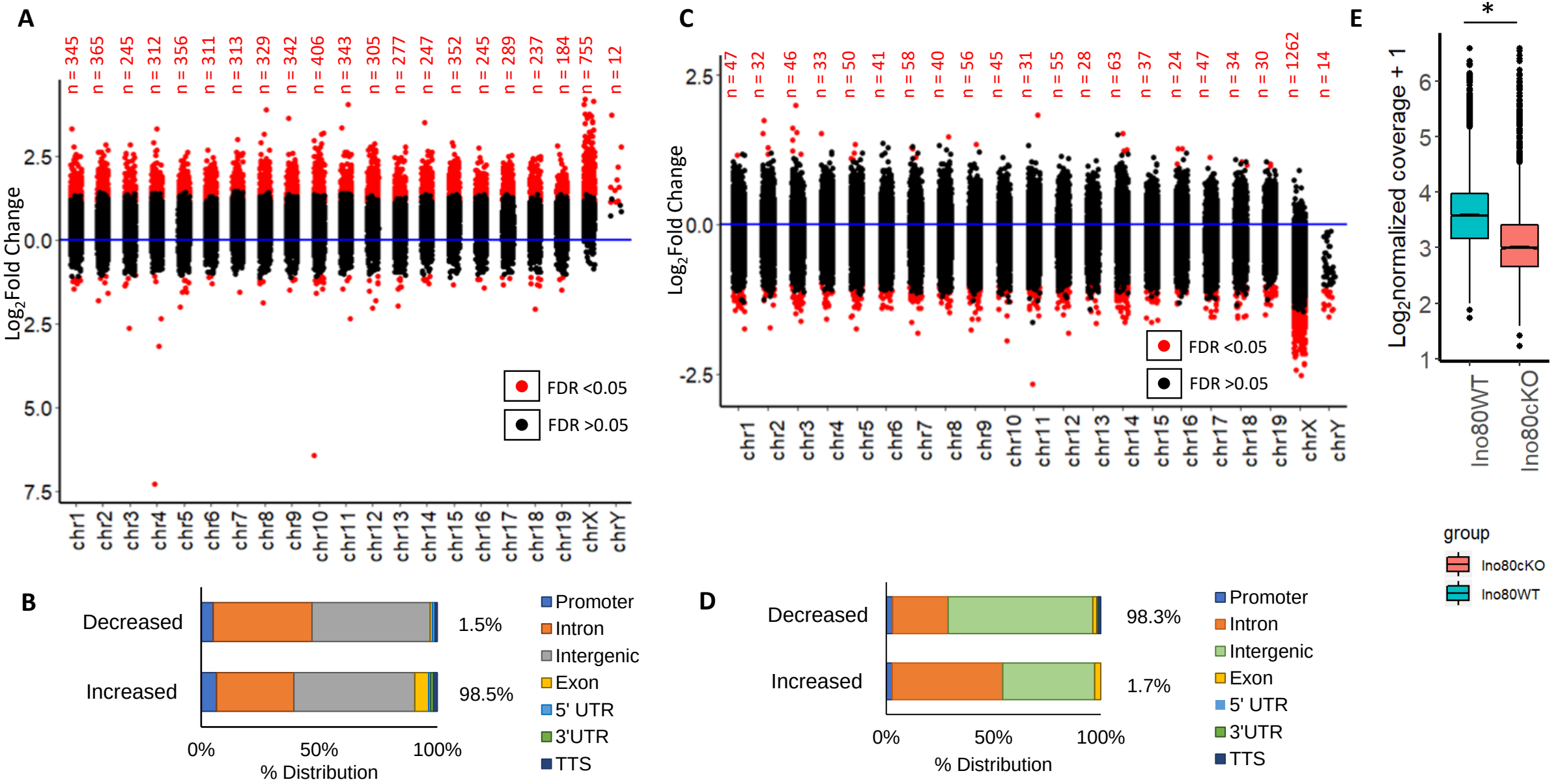
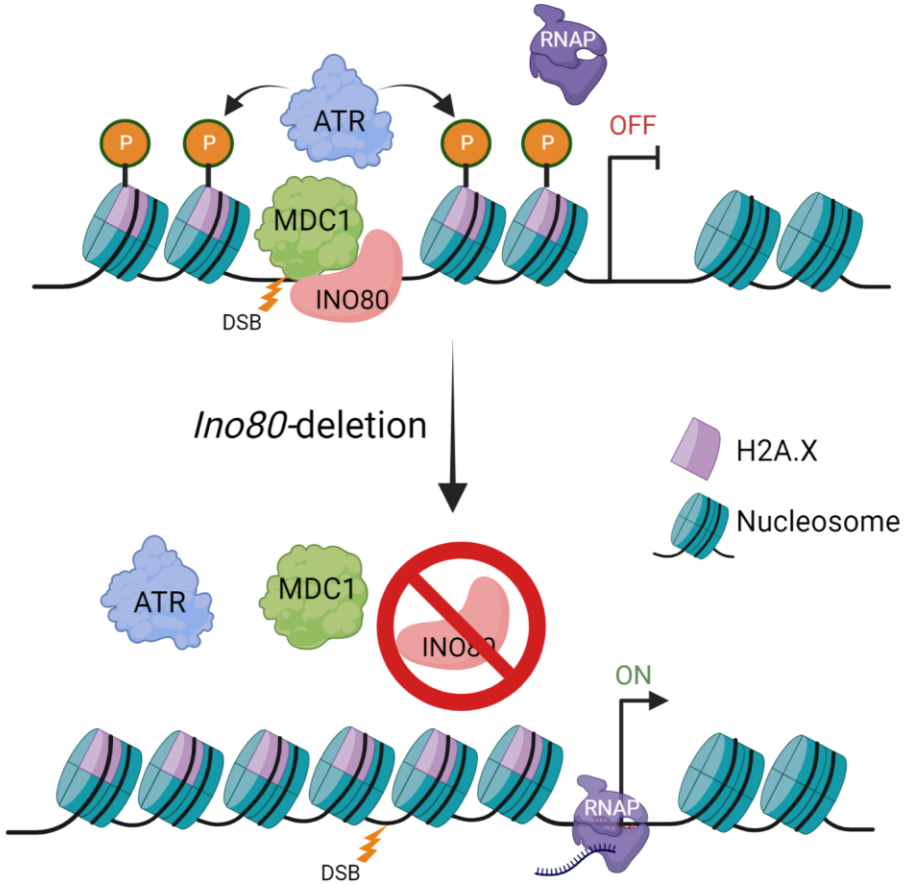
Chakraborty_Figure. 6